ACS APPLIED MATERIALS & INTERFACES

www.acsami.org

Research Article

Formulation of Hierarchical Nanowire-Structured $CoNiO_2$ and MoS_2/$CoNiO_2$ Hybrid Composite Electrodes for Supercapacitor Applications

Zulfqar Ali Sheikh, Dhanasekaran Vikraman, Muhammad Faizan, Honggyun Kim, Sikandar Aftab, Shoyebmohamad F. Shaikh, Kyung-Wan Nam, Jongwan Jung, Sajjad Hussain,* and Deok-Kee Kim*

Cite This: *ACS Appl. Mater. Interfaces* 2024, 16, 10104−10115

Read Online

ACCESS | Metrics & More | Article Recommendations | Supporting Information

ABSTRACT: Hierarchical porous nanowire-like MoS_2/$CoNiO_2$ nanohybrids were synthesized via the hydrothermal process. $CoNiO_2$ nanowires were selected due to the edge site, high surface/volume ratio, and superior electrochemical characteristics as the porous backbone for decoration of layered MoS_2 nanoflakes to construct innovative structure hierarchical three-dimensional (3D) porous NWs MoS_2/$CoNiO_2$ hybrids with excellent charge accumulation and efficient ion transport capabilities. Physicochemical analyses were conducted on the developed hybrid composite, revealing conclusive evidence that the $CoNiO_2$ nanowires have been securely anchored onto the surface of the MoS_2 nanoflake array. The electrochemical results strongly proved the benefit of the hierarchical 3D porous MoS_2/$CoNiO_2$ hybrid structure for the charge storage kinetics. The synergistic characteristics arising from the MoS_2/$CoNiO_2$ composite yielded a notably high specific capacitance of 1340 F/g at a current density of 0.5 A/g. Furthermore, the material exhibited sustained cycling stability, retaining 95.6% of its initial capacitance after 10 000 long cycles. The asymmetric device comprising porous MoS_2/$CoNiO_2$//activated carbon encompassed outstanding energy density (93.02 Wh/kg at 0.85 kW/kg) and cycling stability (94.1% capacitance retention after 10 000 cycles). Additionally, the successful illumination of light-emitting diodes underscores the significant potential of the synthesized MoS_2/$CoNiO_2$ (2D/1D) hybrid for practical high-energy storage applications.

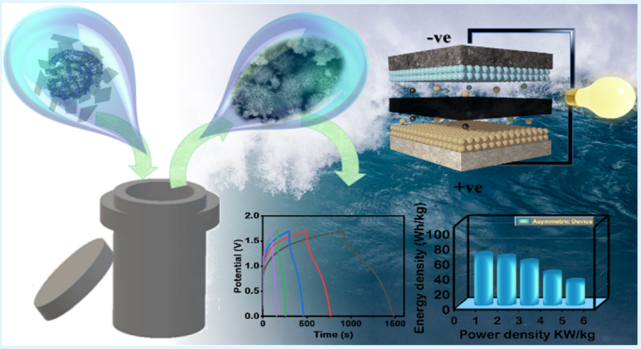

KEYWORDS: *MoS_2, nanowires, supercapacitors, asymmetric, $CoNiO_2$*

1. INTRODUCTION

Electrochemical capacitors (ECs), often referred to as ultra- or supercapacitors, have gained prominence in energy storage/conversion devices in recent times owing to their many advantages, including safety, fast charge/discharge characteristics, higher power density, longer lifecycle, and minimal fabrication/maintenance charge.[1,2] In recent years, numerous research groups have proved that transition metal oxides (TMOs) are considered as likely alternative electrode materials for the oxygen evolution reaction (OER), hydrogen evolution reaction (HER), and ECs/batteries applications.[3,4] Among the series of M−M1 (M, M1 = Co, Ni, Cu, Mo, Fe, and Ni) binary alloys, Co−Ni-based ones have been widely established with attractive electrochemical properties due to the synergistic interactions of Co and Ni, improving the electrical conductivity and boosting the redox reactions in SCs.[5,6] $CoNiO_2$ attracts much attention due to its strong redox activity because of the coexistence of the Ni and Co species, natural abundance, friendly environment, high theoretical capacitance, and sample preparation.[7,8] Several strategies/approaches were utilized to design/prepare some electrocatalysts with unique morphology structures and active sites, including various forms of nanoparticles such as cubes, sheets, wires, tubes, and flakes, to generate the active sites, resulting in improving the electrochemical performances.[9,10] For the rock salt (NaCl)-type $NiCoO_2$ crystal structure, both Ni^{2+} and Co^{2+} coexist in any molar ratio in the crystal structure. These ions are sited in the octahedral voids within the face-centered cubic (FCC) arrangement of oxide ions (O^{2-}).[8] This type of crystal structure is also referred to as a "cation-deficient rock salt" structure. The tetrahedral voids (or sites) within the crystal lattice are empty and also offer free space in the 3D lattice for electron movement and ion/electron transmission.[11] However,

Received: November 28, 2023
Revised: January 26, 2024
Accepted: February 1, 2024
Published: February 16, 2024

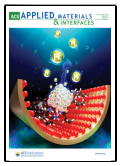

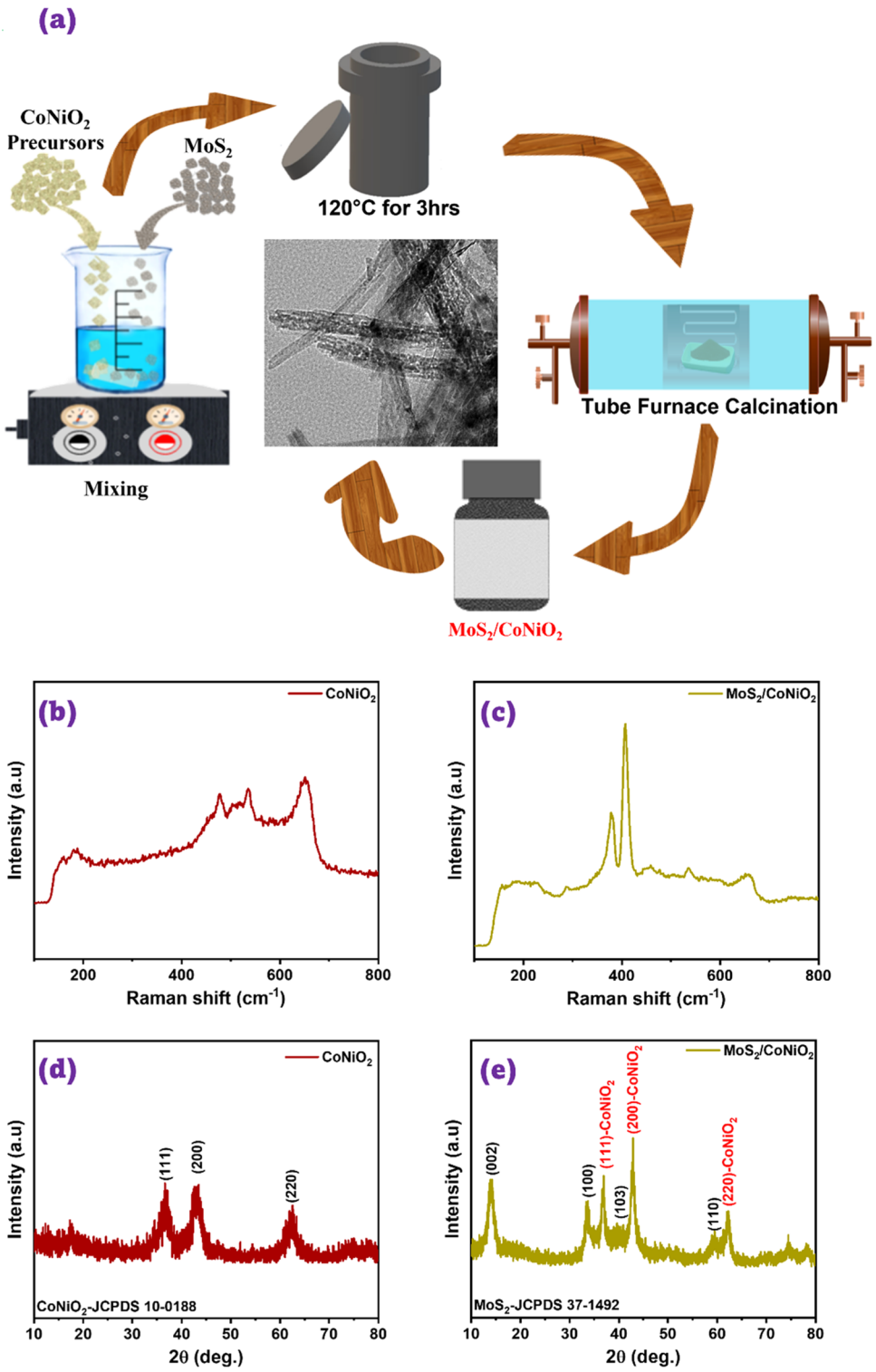

Figure 1. (a) Schematic representation of the interstratification process of a $MoS_2/CoNiO_2$ hybrid. (b) Raman and (d) XRD profiles of $CoNiO_2$. (c) Raman and (e) XRD profiles of the $MoS_2/CoNiO_2$ hybrid.

$CoNiO_2$ still faces problems in electrochemical properties such as low exposure to active sites due to serious agglomeration, low conductivity, and poor stability during charge−discharge cycles.[12,13] Effective approaches were adopted to boost the electrochemical performance by introducing different conductive matrices (carbide/nitride, pure or doped rGO/GO) or semiconductor materials to enable the surface activity of the catalyst for electrochemical properties.[14−16] For example, Pan et al.[15] designed the hierarchical $CoNiO_2$@rGO/NF hybrid to significantly enhance the HER/OER catalytic efficiency. Li et al.[14] synthesized the $CoNiO_2$ microspheres with S additional N-codoped reduced graphene oxide to enhance the electrocatalytic activity and electrical conductivity for the bifunctional (HER and OER) electrocatalysis applications. Leng et al.[17] also demonstrated the hierarchical $NiCoO_2$/rGO/$NiCoO_2$ sandwich nanosheet composite with enhanced specific capacity

https://doi.org/10.1021/acsami.3c17201
ACS Appl. Mater. Interfaces 2024, 16, 10104−10115

and cycling behavior in lithium-ion batteries. The successful synthesis of pure $CoNiO_2$ or a hybrid conductive material, possessing a stable structure and superior catalytic performance, remains a formidable challenge.

Molybdenum disulfide (MoS_2), a group member of layered transition metal dichalcogenide (LTMD) materials, possesses a tunable band gap, exists in different phases (2H, 1T, and 3R), and has active edge sides and mono- or few-layer surfaces.[9,18,19] It consists of a hexagonal lamellar structure with one atom of molybdenum (Mo) and two atoms of sulfur (S) with an interlayer spacing of 0.615 nm. It has recently inspired materials for energy storage applications owing to its intrinsic electronic properties, faster ionic conductivity, and high theoretical capacitance up to 1000 F/g.[20,21] Weak interlayer spaces between layers possessing a longer range of oxidation states from +2 to +6 also support the swift redox faradaic reaction, rendering MoS_2 a potential supercapacitor material.[22,23] The inherent semiconducting nature and susceptibility to restacking/aggregation, oxidation, and termination during cycling contribute to the weak electrochemical characteristics observed in pure layered MoS_2. These factors collectively undermine its candidacy as a stable and enduring electrode material over extended cycling periods. Here, MoS_2 was coupled with $CoNiO_2$ nanowires (NWs) not only to enhance the electronic conductivity but also to prevent the NWs from restacking/aggradation.[9] The hierarchical porous and synergetic coupling effects between MoS_2 and $CoNiO_2$ NWs are believed to generate the active edge sites, contribute to enhancing surface area, and improve conductivity.[24] However, the fabrication/design of $MoS_2/CoNiO_2$ with satisfactory electroactivity and stability is complicated and continues to be a major impediment.

Herein, we demonstrated the preparation of MoS_2 flakes interconnected with 1D $CoNiO_2$ nanowires (NWs, denoted $MoS_2/CoNiO_2$ NWs) through the hydrothermal method. First, in the pursuit of efficient electrolyte penetration, expansion of active sites through a synergistic effect, and facilitation of rapid ionic/electronic diffusion, MoS_2 flakes were employed as a substrate featuring a free-standing architecture composed of $CoNiO_2$ NWs with a porous network. Second, the vertical growth of $CoNiO_2$ NWs on MoS_2 was orchestrated, engineering them into an interconnected nanosheet array to generate abundant structural defects. This strategic design enhances access to the electrolyte throughout the nanosheet, creating enriched porosity that establishes efficient ion transport pathways and numerous electroactive sites. The incorporation of $CoNiO_2$ introduces a multitude of oxidation states, greatly amplifying the capacitive performance through fast, reversible redox reactions. Third, the incorporation of 1D $CoNiO_2$ NWs wrapping around the 2D MoS_2 plays a pivotal role in reinforcing interlayer spacing, ensuring structural integrity, and enhancing electrochemical stability. Capitalizing on these advantages, the electrode composed of 1D $CoNiO_2$ NWs integrated with MoS_2 demonstrates a commendable specific capacitance of 1340 F/g at 0.5 A/g. Furthermore, it exhibits remarkable cycling stability, retaining 95.6% of its initial capacitance after 10 000 cycles. Moreover, a porous $MoS_2/CoNiO_2$//activated carbon (AC) asymmetric supercapacitor (ASC) device exhibits a high-energy density of 93.02 Wh/kg at 0.85 kW/kg as well as superior cyclability with 95.6% of initial capacity after 10 000 cycles. Our work manifests that the fabrication of bimetallic with LTMD materials is an effective approach to improving the performance of supercapacitors.

2. EXPERIMENTAL DETAILS

2.1. Synthesis of $MoS_2/CoNiO_2$. All materials were procured from Sigma-Aldrich, as detailed in the Supporting Information. In this study, a simple hydrothermal technique with a subsequent annealing method was used to prepare the $MoS_2/CoNiO_2$ hybrid composite. The detailed methodology for synthesizing MoS_2 nanostructures is addressed in an earlier study.[9,25] For $MoS_2/CoNiO_2$ hybrid material preparation, initially, blended cobalt acetate $(CH_3CO_2)_2Co$ (3 mM), nickel acetate $Ni(OCOCH_3)_2{\cdot}xH_2O$ (3 mM), and urea (CH_4N_2S, 30 mM) solutions were combined ultrasonically for 45 min with 50 mL of DI water. Thereafter, the mixture was then combined with the as-prepared MoS_2, and it was continuously stirred with a magnetic stirrer for 30 min. This mixture was subsequently placed in a 100 mL autoclave with a Teflon lining. A convection oven set at 120 °C for 3 h was used to heat the sealed autoclave. After carefully washing the resultant black precipitates three times using DI and ethanol, they were vacuum-parched at 60 °C for 12 h. The powder, once parched, was subjected to calcination for 2 h at 400 °C in an atmosphere of argon. The same routine procedure was employed to prepare pure $CoNiO_2$ without containing MoS_2.

2.2. Supercapacitor Device Assembly. The fabricated MoS_2, $CoNiO_2$, and $MoS_2/CoNiO_2$ electrodes' supercapacitor characteristics were investigated by the ZIVE SP1 instrument. In the process of working electrode fabrication, the active components ($CoNiO_2$, MoS_2, and $MoS_2/CoNiO_2$), carbon black, and pVDF were amalgamated within *N*-methyl-2-pyrrolidone, maintaining a precise share of 80:10:10. The resulting slush was deposited onto nickel foam (NF) and exposed to 12 h annealing at 100 °C in an oven. The reference electrode (Hg/HgO), counter electrode (Pt wire), and working electrode ($CoNiO_2$, MoS_2, and $MoS_2/CoNiO_2$-coated NF) were used in the electrolyte of 1 M KOH. A sliced Whatman paper was used as a separator, which was drenched for 8 h in 1 M KOH for ASC device fabrication. A dried Whatman filter paper was inserted between positive ($MoS_2/CoNiO_2$-loaded NF) and negative (activated carbon-coated NF) electrodes. The electrode masses were fixed at 2 and 5 mg/cm^2 for positive and negative electrodes, respectively. The detailed characterization information is provided in S2 in the Supporting Information.

3. RESULTS AND DISCUSSION

3.1. Structural Properties. The synthetic methodology for the $MoS_2/CoNiO_2$ composite is summarized in Figure 1a. Initially, structural analyses were performed to ascertain the formation of $CoNiO_2$ and $MoS_2/CoNiO_2$. Figure 1b shows the Raman spectrum of $CoNiO_2$ structures, which produces broad peaks at 476, 536, and 664 cm^{-1}, corresponding to the isostructural forms of NiO_2, $CoNiO_2$, and CoOOH, respectively.[26,27] Figure 1c shows the Raman profile of $MoS_2/CoNiO_2$ hybrid structures. The couple of MoS_2 characteristic bands at E_{2g} (382.1 cm^{-1}) and A_{1g} (407.2 cm^{-1}) modes are enabled in the hybrid structure in addition to the NiO_2, $CoNiO_2$, and CoOOH peaks in the $MoS_2/CoNiO_2$ Raman profile. X-ray diffraction (XRD) studies were formed for the $CoNiO_2$ and $MoS_2/CoNiO_2$ hybrids, as shown in Figure 1d,e, respectively. The notable peaks at 36.74, 42.92, and 62.17° are in accordance with the (111), (200), and (220) planes, respectively, which are related to the cubic $NiCoO_2$ phase (JCPDS 10-0188) for the $CoNiO_2$ NWs structure. For the $MoS_2/CoNiO_2$ hybrid, the MoS_2-related diffraction peaks at 14.39, 32.91, 39.69, and 58.76° are attributed to the reflection planes (002), (100), (103), and (110). These values aligned well with the MoS_2 hexagonal phase as documented by JCPDS 37-1492. The determined mean crystallite sizes, as

https://doi.org/10.1021/acsami.3c17201
ACS Appl. Mater. Interfaces 2024, 16, 10104−10115

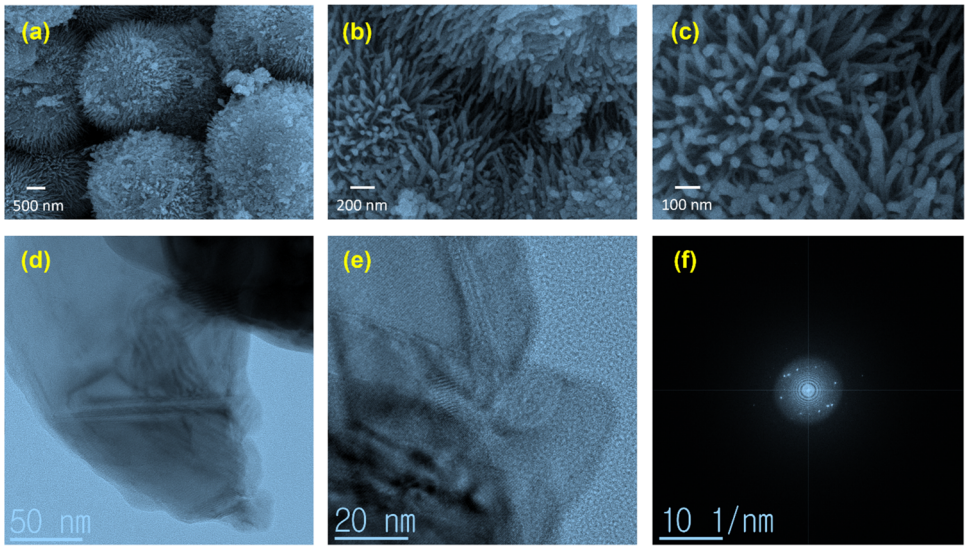

Figure 2. Microscopy images of $CoNiO_2$: (a–c) different magnifications of FESEM micrographs, (d, e) different magnifications of TEM micrographs, and their (f) FFT pattern.

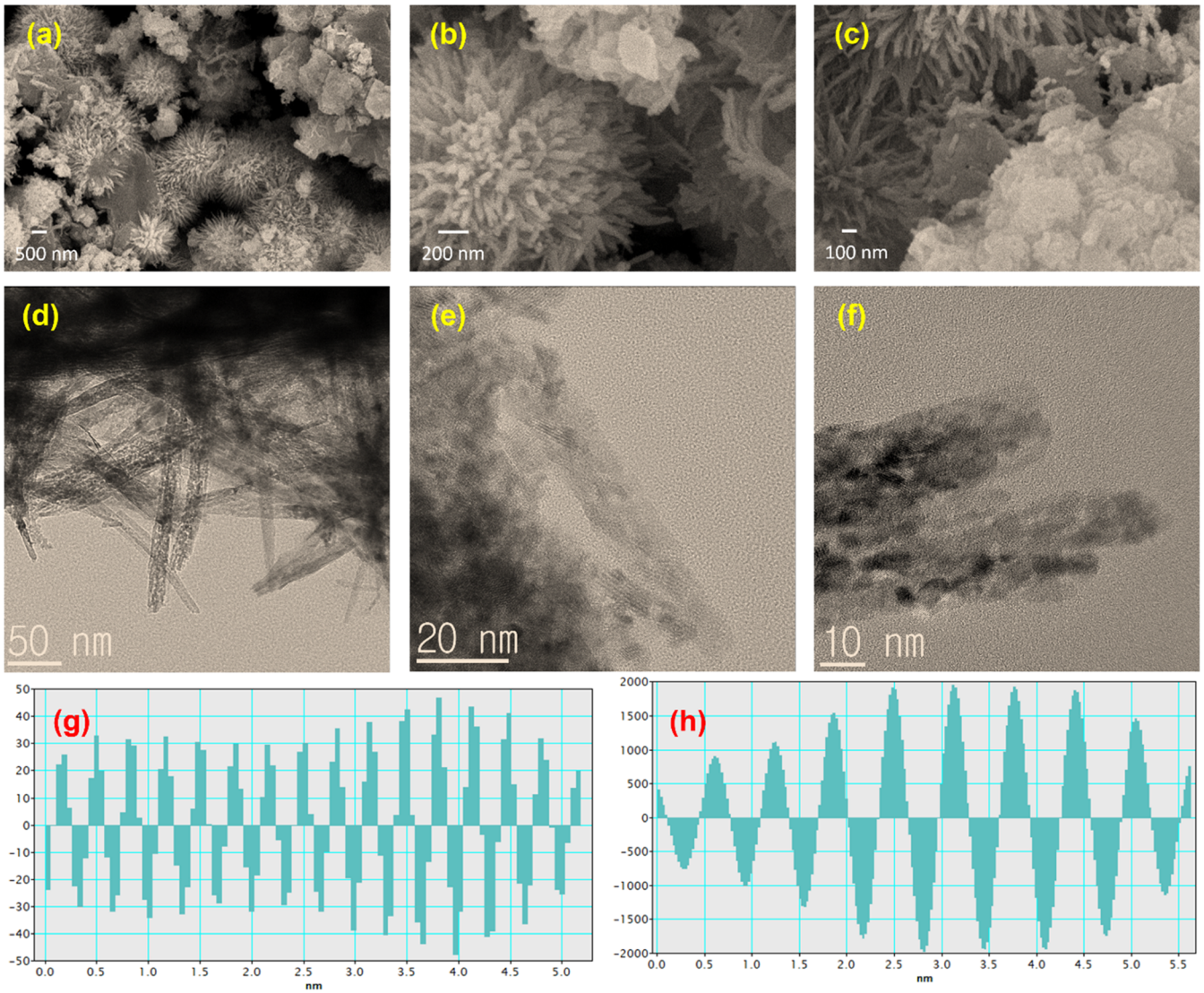

Figure 3. Microscopic images of the $MoS_2/CoNiO_2$ hybrid: (a–c) different magnifications of FESEM micrographs, (d–f) different TEM magnifications, and phase profiles of (g) MoS_2 and (h) $CoNiO_2$ lattices.

https://doi.org/10.1021/acsami.3c17201
ACS Appl. Mater. Interfaces 2024, 16, 10104–10115

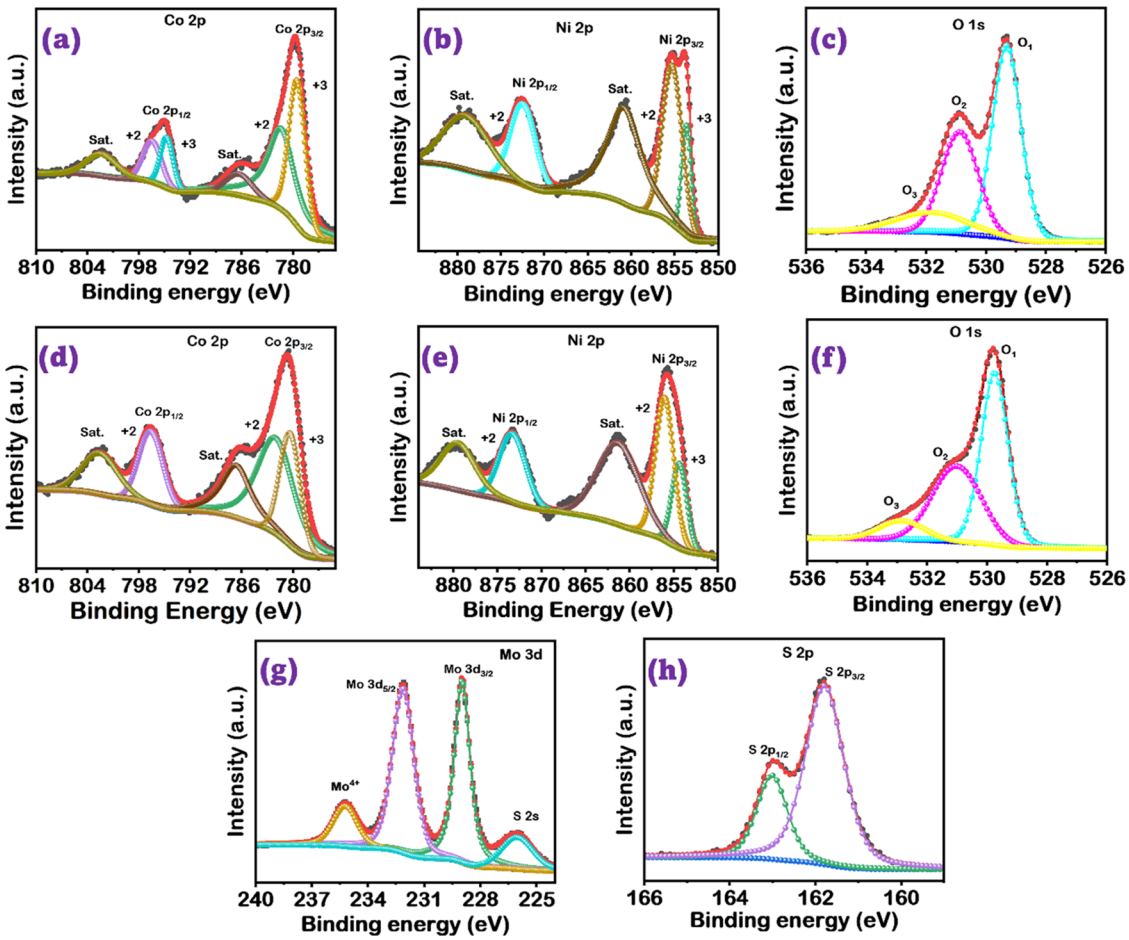

Figure 4. XPS spectra of $CoNiO_2$: (a) Co 2p, (b) Ni 2p, and (c) O 1s; $MoS_2/CoNiO_2$ hybrid: (d) Co 2p, (e) Ni 2p, (f) O 1s, (g) Mo 3d, and (h) S 2p.

determined through the Scherrer equation,[28] for MoS_2, $CoNiO_2$, and the $MoS_2/CoNiO_2$ hybrid structure were 3.6, 4.7, and 6.1 nm, respectively. In addition, $NiCoO_2$-related lattice planes are observed for the $MoS_2/CoNiO_2$ hybrids. The collectively produced synergistic vibrational modes strongly ascertained the $MoS_2/CoNiO_2$ hybrid formation.

XPS was engaged to probe the elemental compositions and oxidation states present in both $CoNiO_2$ and the $MoS_2/CoNiO_2$ hybrid structure. The survey spectrum (Figure S1a,b) exhibits the $CoNiO_2$ (Co, Ni, and O), as well as the simultaneous existence of Ni, Co, Mo, S, and O elements in the $MoS_2/CoNiO_2$. Figure 2a–c shows the Co 2p, Ni 2p, and O 1s binding energy profile of $CoNiO_2$ NWs, respectively. Co 2p reveals the main couples at 795.1 and 779.6 eV corresponding to Co $2p_{1/2}$ and Co $2p_{3/2}$ states, respectively, confirming the metal Co^0 state presence (Figure 2a). The Co^{2+} states are sited at 801.1 and 783.3 eV, whereas Co^{3+} duos are placed at 799.3 and 781.4 eV (Figure 2a).[29,30] From the Ni 2p region (Figure 2b), a couple of core peaks were detected at 856.6 for Ni $2p_{3/2}$ and 874.2 eV for Ni $2p_{1/2}$. Also, the duos at 859.2 and 877.3 eV are credited to Ni^{3+} $2p_{3/2}$ and $2p_{1/2}$ states, respectively. It is imperative to highlight that the observed high binding energy peak duos can emerge from the nickel (hydro)oxide.[26,31] Figure 2c displays the O 1s profile, which defines the characteristic oxide- and defective oxide-related peaks from the $CoNiO_2$ phase.[9,32]

Figure 2d–h shows the Co 2p, Ni 2p, O 1s, Mo 3d, and S 2p binding energy profiles of $MoS_2/CoNiO_2$ hybrid structures, respectively. Figure 2d displays the XPS profile of the Co 2p region for $MoS_2/CoNiO_2$, showcasing the duos cited at 794.6/779.7 eV and 798.8/782.5 eV. These peaks are ascribed to the Co $2p_{1/2}$/Co $2p_{3/2}$ states of Co^{3+} and Co^{2+} species, respectively, appearing at higher binding energies (785.8/803.3 eV) by satellite (Sat.) peaks, which indicates the coexisting configuration of Co^{3+} and Co^{2+} in the $MoS_2/CoNiO_2$ hybrid.[33] Figure 2e demonstrates the Ni 2p profile for $MoS_2/CoNiO_2$, which explores the distinct peaks at 875.5 eV (Ni^{2+} $2p_{1/2}$) and 857.9 eV (Ni^{2+} $2p_{3/2}$). Notably, the subsequent satellite waves at 881.5 and 862.9 eV signify the existence of Ni–Mo. Moreover, we have explored the additional couples at 853.9 eV (Ni^{3+} $2p_{3/2}$) and 871.3 eV (Ni^{3+} $2p_{1/2}$).[33] It was noted that the binding energy of Co 2p and Ni 2p are shifted positively by 0.8 and 0.5 eV compared to pure $CoNiO_2$. Figure 2f displays the O 1s profile, which describes the characteristic oxide- and defective oxide-related peaks from the $CoNiO_2$ phase. From the Mo 3d region of hybrids (Figure 2g), the XPS profile defines the Mo $3d_{3/2}$ (232.5 eV) and Mo $3d_{5/2}$ (229.3 eV) peaks corresponding to Mo^{4+}, along with a small pathetic sulfur peak (S 2s) at 226.5 eV and an oxidate Mo^{6+} peak (236.1 eV). Figure 2h exposes the S 2p orbital doublets that appeared at $2p_{1/2}$–163.1 and $2p_{3/2}$–162.1 eV.[34] All of the inclusively obtained element binding energy profiles witness the formation of the $MoS_2/$

https://doi.org/10.1021/acsami.3c17201
ACS Appl. Mater. Interfaces 2024, 16, 10104–10115

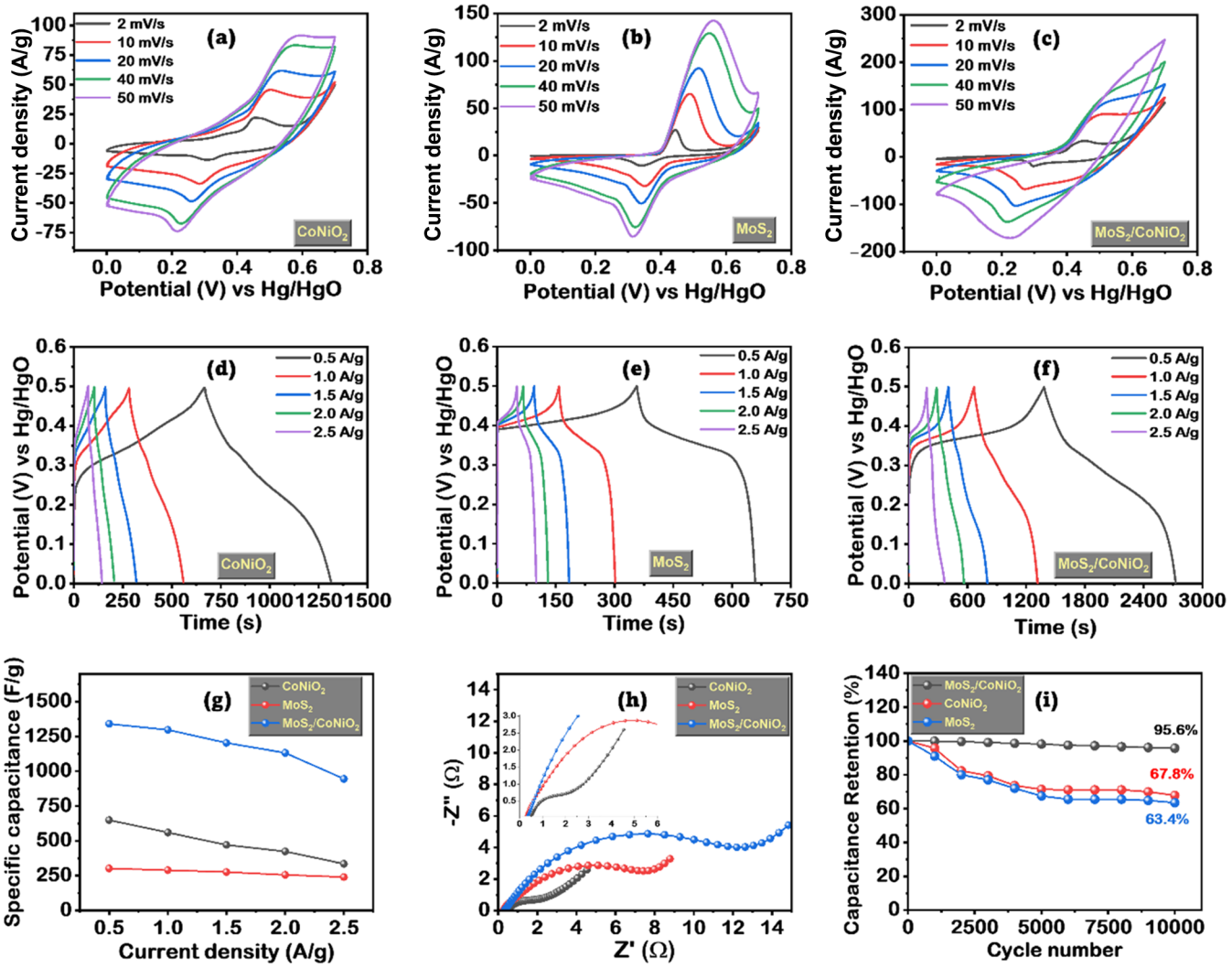

Figure 5. Half-cell supercapacitor characteristics: CV curves acquired at a scan rate of 2−50 mV/s of (a) $CoNiO_2$, (b) MoS_2, and (c) MoS_2/$CoNiO_2$ hybrid. GCD profiles at various applied currents for (d) $CoNiO_2$, (e) MoS_2, and (f) MoS_2/$CoNiO_2$ hybrid electrodes. (g) specific capacitances of $CoNiO_2$, MoS_2, and MoS_2/$CoNiO_2$ electrodes at various applied currents. (h) EIS pattern of different electrodes with an insert of zoom image. (i) 10 000 cycle capacitance retention profiles for $CoNiO_2$, MoS_2, and MoS_2/$CoNiO_2$ hybrid electrodes.

$CoNiO_2$ hybrid. These results also impact the redistribution of charges across the interfaces of each material, which supports the improvement of catalytic activity and durability.

Scanning electron microscopy (SEM) and transmission electron microscopy (TEM) experiments were done to examine the morphological characteristics of $CoNiO_2$ and the MoS_2/$CoNiO_2$ hybrid. Figure 3a−c shows the $CoNiO_2$ NWs SEM images with various magnifications. The outcomes demonstrated that the protruding of well-ordered NWs-modeled grains from the irregular surface clusters or bunches resembled certain features of desert plant grains (Figure 3a). The magnified micrograph of $CoNiO_2$ illustrates the growth of arranged NWs-designed granules. Figure 3d−f demonstrates the various resolutions of the TEM images for the $CoNiO_2$ nanostructures. The picture explores the accumulated wire-shaped grains. The observed FFT pattern (Figure 3f) clearly explores the polycrystalline lattice planes in $CoNiO_2$. Figure 4 designates the SEM and TEM images of the MoS_2/$CoNiO_2$ hybrid. The observed low-magnification SEM image (Figure 4a) shows broken $CoNiO_2$ NWs distributed around the petal-shaped MoS_2 along with the blended morphological characteristics with numerous nanoparticles. Multiple channels/edges exist in NWs (Figure 4b,c), which provide multiple channels/edges and a large surface area to enhance the conductivity and shrink the structural collapse during electrochemical kinetics. The intricate interplay between MoS_2 and $NiCoO_2$ in hybrid formation is evident in the detailed images at high magnification. Additionally, to analyze the MoS_2/$NiCoO_2$ hybrid constituents, energy-dispersive spectroscopy (EDS) was carried out. Figure S2a−g demonstrates the element mapping images of the MoS_2/$NiCoO_2$ hybrid, illustrating the elements' uniform distribution across the surface. Through elemental evaluation, it was determined that the MoS_2/$NiCoO_2$ hybrid comprised Ni (14.5%), Co (13.68%), O (45.18%), Mo (12.07%), and S (14.53%). The TEM images in Figure 4d−f depict varying resolutions of MoS_2/$NiCoO_2$ hybrid nanostructures. The attachment of NW grains with the layered architecture is clearly explored in the TEM image, as shown in the low-amplification image. The high-resolution imagery obviously explores the decorated, well-dispersed NWs on the layered structures. The phase spectra used to reveal the lattice organization space by the spot mask mode, as shown in

https://doi.org/10.1021/acsami.3c17201
ACS Appl. Mater. Interfaces 2024, 16, 10104−10115

Figure 4g,h, explore the (113) lattice plane of $CoNiO_2$ and the (002) MoS_2 crystal plane, respectively.[9] The observed results clearly demonstrate the formulation of $CoNiO_2$ as well as the formation of the $MoS_2/CoNiO_2$ hybrid.

To explore changes in the surface properties of $CoNiO_2$, MoS_2, and $MoS_2/CoNiO_2$ hybrid, we conducted Brunauer–Emmett–Teller (BET) adsorption/desorption isotherm analysis.[4] The BET results unveiled that the $MoS_2/CoNiO_2$ hybrid demonstrated a substantially porous structure, boasting a specific surface area of approximately 29.69 m^2 g, surpassing the values for MoS_2 (~8.73 m^2/g) and $CoNiO_2$ (~19.26 m^2/g) shown in Figure S3a. This enhancement can be attributed to the $CoNiO_2$ embedded in the LTMDs layer. Figure S3b illustrates the Barrett–Joyner–Halenda (BJH) pore-size distribution curves for MoS_2, $CoNiO_2$, and $MoS_2/CoNiO_2$ hybrid. The determined mean pore diameters were 46.42 nm for MoS_2, 15.25 nm for $CoNiO_2$, and 11.92 nm for $MoS_2/CoNiO_2$ hybrids. The observed high surface area of $MoS_2/CoNiO_2$ hybrids leads to the presence of abundant active sites. The connection of $CoNiO_2$ NWs to the MoS_2 nanohybrids facilitates the generation of active sites and various transport channels, promoting easy accessibility. This structural configuration significantly enhances ion/electron diffusion.

3.2. Half-Cell Measurement. The electrochemical efficacy of all fabricated samples was examined by employing a three-electrode configuration in a 1 M KOH solution at room temperature via CV and GCD techniques. For the detailed comparison, as-prepared MoS_2 nanosheets were used for electrochemical measurements, which were prepared by hydrothermal processes as noted in the existing literature.[25] Figure S4 shows the SEM data of as-prepared MoS_2 layered structures. Figure S5a depicts the cyclic voltammetry (CV) of the $MoS_2/CoNiO_2$ hybrid across varying voltage intervals (0.5–0.7 V). By opting for a 0.7 V potential window, the CV profiles of $CoNiO_2$, MoS_2, and $MoS_2/CoNiO_2$ hybrid electrodes were obtained, employing a constant scan rate of 50 mV/s within the potential range from 0 to 0.7 V as presented in Figure S5b. The MoS_2 electrode reveals the battery-type characteristics via redox reactions between Mo^{4+} and Mo^{6+} from the interface of MoS_2,[35] whereas the $CoNiO_2$ curve possesses pseudocapacitive characteristics with a smaller pair of redox peaks, contributing to the behavior of M–O/M–O–OH (M = Co, Ni) or Ni^0/Ni^{2+} and Co^0/Co^{2+} faradaic reactions transferred by hydroxide ions (OH^-) from the KOH solution,[36] undergoing the following faradic reactions:

$$CoNiO_2 + OH^- + H_2O \rightleftarrows NiOOH + 2CoOOH + 4e^- \quad (1)$$

$$CoOOH + OH^- \rightleftarrows 2CoO_2 + H_2O + e^- \quad (2)$$

$MoS_2/CoNiO_2$ hybrid electrodes exhibited a significantly greater integrated area compared to the MoS_2 or $CoNiO_2$ electrodes, indicating that each component contributes to the capacity of the mixing electrode. In addition, the reduction peaks of $CoNiO_2$, MoS_2, and $MoS_2/CoNiO_2$ hybrid electrodes were displayed at 0.213, 0.312, and 0.289 V versus Hg/HgO with a scan rate of 50 mV/s. The oxidation peaks corresponding to these were identified at 0.572, 0.561, and 0.627 V versus Hg/HgO.

Figure 5a–c shows different scan rates, such as 2, 10, 20, 40, and 50 mV/s, of the recorded CV plots for $CoNiO_2$, MoS_2, and $MoS_2/CoNiO_2$ hybrid. No distortion in the CV shape was observed, leading to high reversibility. In addition, the separation of the redox peak increased with the increase in scan rate, presenting high catalytic activity. The distinct positions of redox peaks in the CV curves for $CoNiO_2$, MoS_2, and $MoS_2/CoNiO_2$ can be attributed to three primary factors: (i) Variations in the composition/stoichiometric ratio and chemical redistribution states of Co or Ni or Mo/S ions in the material product led to diverse Faraday redox reactions happening on the electrode surfaces. (ii) The electrodes exhibit discrepancies in the number of sufficient exposure active sites with plenty of nucleation cores due to their differences in specific surface area/shape and unique morphology having porosity/NW or open nanostructures, resulting in varied sizes and positions in the redox peaks of CV curves. (iii) The strongly embedded $CoNiO_2$ NWs on MoS_2 flakes behave as efficient promoters to enhance rapid electron transfer between the conductive MoS_2 porous skeleton and the active NW species. In addition, the synergistic effect of the 1D@2D heterostructure is accountable for the superior electrochemical efficiency.

Leveraging the power law, we scrutinize the interrelated influences of electrodes designed for battery-type or EC applications, specifically focusing on $CoNiO_2$, MoS_2, and the $MoS_2/CoNiO_2$ hybrid structure. The equation employed for this analysis is outlined as follows.

$$i = a\nu^b \quad (3)$$

Here, i represents the observed peak current, and ν denotes the sweep rate. Both a and b are adjustable parameters. In a power law, capacitive-controlled current dominates the charge storage mechanism (ECs type) when b equals 1. Conversely, in a different scenario where b is set to 0.5, the charge storage mechanism is influenced by the diffusion-controlled current (battery type).[37]

Figure S6a–c displays the logarithmic relationship between current density and scan rate for $CoNiO_2$, MoS_2, and the $MoS_2/CoNiO_2$ hybrid structure samples. The calculated "b" values for these samples are 0.55, 0.51, and 0.56, respectively. Across scan rates ranging from 2 to 50 mVs^{-1}, the "b" values for all electrodes fall between 0.5 and 1. This observation suggests that the electrochemical charge storage mechanism involves a combination of diffusion-controlled and ECs-controlled behaviors.

Additionally, we employ a revised power law (eq 4) to assess the quantity of charge retained through the surface ECs and bulk battery-type mechanisms

$$I_p = C_s\nu + C_b\nu^{1/2} \quad (4)$$

Here, ν represents the scan rate, I_p denotes the peak current density, and $C_b\nu^{1/2}$ and $C_s\nu$ correspond to the current associated with the bulk process (I_{bulk}) and surface SCs mechanism ($I_{surface}$), respectively.[38] The current density obtained from the battery's bulk I_{bulk} and the SCs surface $I_{surface}$ mechanisms is illustrated in Figure S6d for various scan rates ranging from 2 to 50 mV/s. Typically, MoS_2 is recognized as an EC material, while $CoNiO_2$ serves as a battery electrode material. The comprehensive findings reveal that the obtained values predominantly align with the characteristics of the battery-like bulk process and, to some extent, encompass the surface pseudocapacitive process.

Galvanostatic charge–discharge (GCD) curves for $CoNiO_2$, MoS_2, and $MoS_2/CoNiO_2$ hybrid were recorded at a current density at 0.5 A/g for comparison in the potential range of 0–

https://doi.org/10.1021/acsami.3c17201
ACS Appl. Mater. Interfaces 2024, 16, 10104–10115

0.5 V, as shown in Figure S5c. The estimated, as reported in the literature,[4,39] C_S values of the fabricated $CoNiO_2$, MoS_2, and $MoS_2/CoNiO_2$ electrodes at 0.5 A/g applied current were 649, 302, and 1340 F/g, respectively. The nonlinear and symmetric GCD curves of these electrodes imply their commendable chemical reversibility. The clearly defined battery-like behavior of $CoNiO_2$, MoS_2, and $MoS_2/CoNiO_2$ electrodes is exhibited by charge/discharge plateaus, which aligns with results obtained from CV. In addition, the $MoS_2/CoNiO_2$ electrode demonstrates a discharge duration longer than those of the other electrodes, which indicates its superior specific capacity to the other two electrodes.

The GCD profiles of $CoNiO_2$, MoS_2, and $MoS_2/CoNiO_2$ at different applied currents (0.5−2.5 A/g) are shown in Figure 5d−f, respectively. The specific capacitance (C_s) was determined through the computation of GCD profiles, as detailed in eq S1 in the Supporting Information. The estimated C_s of the $CoNiO_2$ electrode at applied currents of 0.5, 1, 1.5, 2, and 2.5 A/g were 649, 560, 471, 424, and 335 F/g, respectively; C_s values of MoS_2 were 302, 290, 276, 256, and 240 F/g, and those of the $MoS_2/CoNiO_2$ electrode were 1340, 1298, 1203, 1132, and 945 F/g, respectively, as display in Figure 5g. The GCD profiles of MoS_2 and $MoS_2/CoNiO_2$ electrodes appeared to be nonlinear symmetric charge/discharge curves, proving the battery-type redox behaviors shown in Figure 5d−f. It is noteworthy that the $MoS_2/CoNiO_2$ hybrid has a higher Cs value than other electrodes due to the seamless heterointerfaces and synergistic effect of $CoNiO_2$ and MoS_2. Additionally, MoS_2 is beneficial to reducing interfacial contact and enhancing electron transportation and significant specific surface area in the composite electrode. The $MoS_2/CoNiO_2$ hybrid electrode exhibited enhanced charge storage characteristics in comparison to previously documented TMO-LTMDs in the literature (Table S1). Notably, it outperformed materials like $Co_xMo_{1-x}S_2/C$ (C_s-184 F/g at 0.5 A/g), 1T/2H MoS_2 (C_s-742 F/g at 5 mV/s),[40] (C_s−Co_4S_3/Ni_3S_2@MoS_2 core−shell nanosheet at 1238 F/g at 1 A/g),[41] $NiMoO_4$@Ni_9S_8/MoS_2 (373.4 F/g at 10 A/g),[42] MXene-MnO_2−CoNi LDH (C_s-922 F/g at 1 A/g),[43] MoS_2/VS_2 nanourchins-rGO (C_s-460 F/g at 0.5 A/g),[44] and Cr-doped $MoS_2/CuCo_2S_4$ (C_s-1324.08 C/g at 4 A/g),[45] as summarized in Table S1.

Moreover, the electronic conductivity and capacitive behavior of the fabricated electrodes were probed by the EIS study. Figure 5h represents the combined Nyquist plot for $CoNiO_2$, MoS_2, and $MoS_2/CoNiO_2$ hybrid. Additionally, Figure S7a−c presents separate Nyquist plots for $CoNiO_2$, MoS_2, and $MoS_2/CoNiO_2$ hybrid, each accompanied by its corresponding circuit diagram. The charge transfer resistance (R_{ct}) values were derived for $CoNiO_2$, MoS_2, and $MoS_2/CoNiO_2$ hybrid as 8.5, 5, and 1.2 Ω, respectively. The incorporation of MoS_2 in $CoNiO_2$ to synthesize the $MoS_2/CoNiO_2$ hybrid composite electrode led to an enhancement in conductivity and a reduction in R_{ct}, which led to rapid ionic/electrical diffusion and an increase in the value of C_s as well as an improvement in excellent rate capability compared to the $CoNiO_2$ and MoS_2 electrodes. Further, the cyclic stability of all electrodes was taken for 10 000 charge−discharge cycles under a 5 A/g current density and sustained their capacitance up to 95.6% for the $MoS_2/CoNiO_2$ hybrid composite, which is better as compared to pure $CoNiO_2$ (67.8%) and MoS_2 (63.4%), as shown in Figure 5i. The $CoNiO_2$ NWs are intimately affixed to the MoS_2 flakes, ensuring superior adhesion and intimate interfacial contact. This establishment of a distinctive robust framework serves to effectively mitigate the corrosion and collapse tendencies within the nanostructured electrode while repetitive cycling processes. Moreover, the $CoNiO_2$ NWs possess an inherent porous architecture, facilitating increased exposure of active materials to the electrolyte solution. This design minimizes the diffusion distance for ions, affording a substantial number of accessible active sites, thereby contributing to enhanced stability. Furthermore, Figure S8 specifically highlights the 1st, 2500th, 5000th, 7500th, and 10 000th GCD cycles of the $MoS_2/CoNiO_2$ electrode. Figure S9 provides valuable insights into the morphological changes occurring in the $MoS_2/CoNiO_2$ hybrid electrode upon electrochemical testing. The morphology of the $MoS_2/CoNiO_2$ electrode was assessed following an extended cycling process of 10 000 cycles. The SEM and EDS mapping results, along with corresponding analyses, are depicted in Figure S9a−h, both initially and after subjecting the electrode to 10 000 cycles of GCD. Notably, the hollow core−shell structure of the electrode is observed to endure without evident collapse after 10 000 cycles of GCD, as shown in Figure S9e,f. However, in certain regions, oxidation is apparent, attributed to sulfur-related processes and the occurrence of some fractured $CoNiO_2$ nanowires compared to the original morphology. To validate these observations, EDS analysis was employed to quantify the elemental composition. As illustrated in Figure S9c,g, there is no significant reduction in the percentage of each element content before and after the cycling performance, respectively. This underscores the resilience of the hierarchical core−shell hollow architecture of the electrode, indicating its superior performance over the extended cycling duration. This capacitance retention surpasses or closely aligns with the majority of the previously fabricated 2D TMDs or oxide-based ECs (Table S1).[46−49] The hierarchical $MoS_2/CoNiO_2$ hybrid composite possesses several advantages in terms of outstanding rate capabilities and cyclic stability. These advantages stem from the unique properties and synergistic effects of the combined materials. Here are some of the key advantages: (1) $CoNiO_2$ NWs grown on the MoS_2 substrate can provide a high surface area-to-volume ratio, which is advantageous for electrochemical reactions. The nanowire structure allows for greater revealing of active sites, improving the overall electrochemical results of the composite and thus improving the energy density of the capacitor.[7] (2) The porous, enriched $CoNiO_2$ NW electrode material possesses a lighter weight than the solid one. The reduced weight of the material on the electrode, increased surface area, enhanced ion diffusion, and better electrolyte accessibility lead to enhanced energy density and power density of the ECs.[4] (3) The presence of a hollow NW structure creates a physical barrier among the electrode material active surface (NWs) and the electrolyte.[21] This isolation helps to prevent a direct interaction between the material and the potentially corrosive electrolyte, reducing the risk of chemical reactions that can lead to material degradation or corrosion and can also affect ion diffusion pathways. (4) $CoNiO_2$ NWs grown on the MoS_2 nanoflakes create fluffy nanosheet configurations. Both materials actively engage in storing charge through quick and reversible redox reactions at the electrode−electrolyte interface and rapid surface adsorption/desorption of ions and facilitate ion transport, greatly refining and synergistically enhancing the energy storage impact of these materials. (5) The distinct heterostructure not only amalgamates the individual inherent properties of $CoNiO_2$ NWs and MoS_2 nanoflakes but also accelerates the

https://doi.org/10.1021/acsami.3c17201
ACS Appl. Mater. Interfaces 2024, 16, 10104−10115

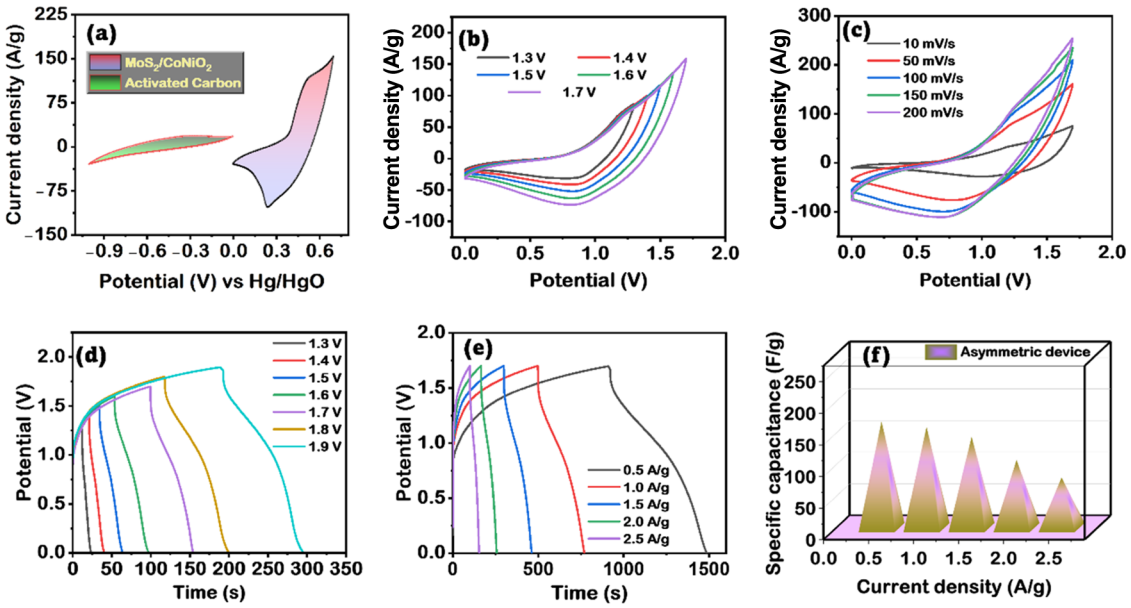

Figure 6. $MoS_2/CoNiO_2$//AC-configured asymmetric supercapacitor characteristics: (a) CV curves of activated carbon and $MoS_2/CoNiO_2$. (b) CV curves of the ASC devices at different voltage intervals (1.3−1.7 V). (c) CV curves of the ASC device at different sweep rates (10−200 mV/s) at a voltage window of 1.7 V. (d) GCD profiles of the ASC device with different voltage windows at 2.5 A/g current density. (e) GCD curve of the ASC device at different current densities (0.5−2.5 A/g). (f) Capacitances of the constructed ASC device at different applied currents.

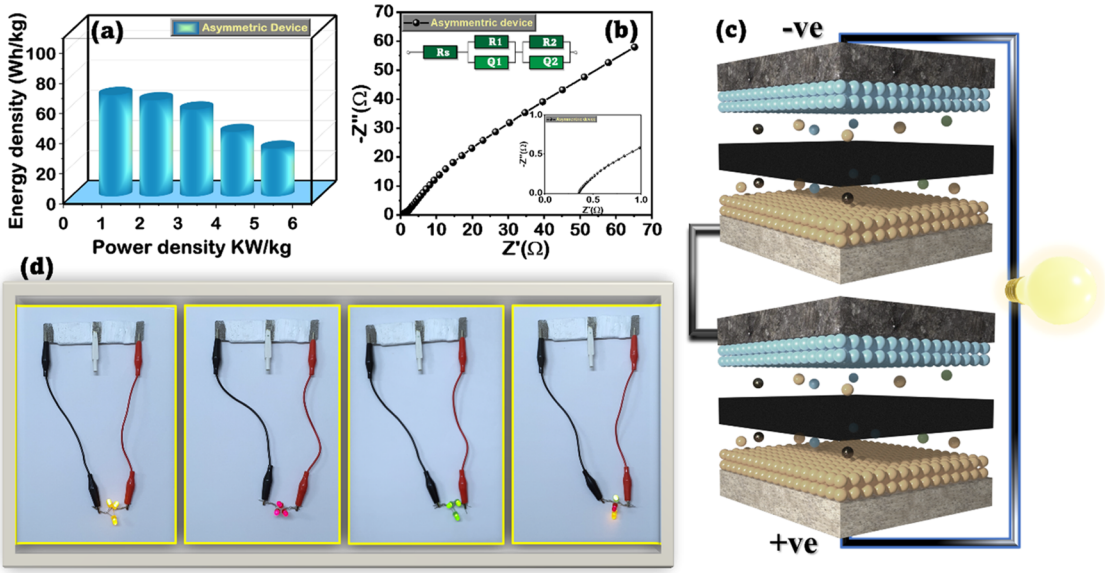

Figure 7. (a) Ragone plots and (b) EIS results of the constructed ASC device (inset: circuit diagram). (c) Systematic representation of the asymmetric device structure using $MoS_2/CoNiO_2$. (d) Light emission devices (LEDs) of pink, red, green, and mixed colors of the assembled asymmetric device for 20 min.

easy ion/electron transfer by the effective interfacial engineering developed among them, activating additional active sites and faster charge/discharge rates and greatly enhancing the cycling stability/longevity. Additionally, the electrochemical characteristics of activated carbon (AC) by half-cell supercapacitors are illustrated in Figure S10. Figure S10a displays the CV curves obtained at scan rates ranging from 2 to 50 mV/s within a potential window from 0 to −1 V. In Figure S10b,c, the GCD profiles and their volumetric capacitance are presented at current densities between 0.5 and 2.5 A/g, respectively. The observed volumetric capacitance value of 116.5 F/cm^{-2} at 0.5 A/g current density is ascertained by the sustained capacitance nature of the prepared activated carbon negative electrode.

3.3. Asymmetric Supercapacitors. To assess the practical application performance of $MoS_2/CoNiO_2$, the asymmetric supercapacitor (ASC, two-electrode geometry) was fabricated using MoS_2@$CoNiO_2$ and active carbon (AC) as the positive and negative electrodes, respectively, and KOH-dipped filter-based paper was used as the electrolyte (Figure 6a). The potential windows of the $MoS_2/CoNiO_2$ and ASC were concluded with the CV technique. The CV curve was taken from 0 V to different high potential windows of 1.3−1.7 V to analyze the charge storage kinetics of assembled device. Up to the CV curve at 1.7 V, no pinch or curling up was

https://doi.org/10.1021/acsami.3c17201
ACS Appl. Mater. Interfaces 2024, 16, 10104−10115

observed. Thus, the highest potential gap of $MoS_2/CoNiO_2$//AC was 0−1.7 V at a scan rate of 10 mV/s (Figure 6b). CV curves display nearly rectangular-like loops with redox peaks, showing that both EDLC and battery-type work together on the ASC device. CV curves were also performed at different scan rates of 10−200 mV/s in a working potential window of 0−1.7 V, as shown in Figure 6c. No significant shift/distortion confirms the excellent electrochemical reversibility due to favorable ionic/electronic transfer behaviors. The GCD curves were also collected at fixed current densities (2.5 A/g) for different potential windows (1.3−1.9 V), as shown in Figure 6d, which shows quasi-triangular shapes associated with EDLC or the possibilities of a pseudocapacitance mechanism, implying a quick charge−discharge process. Figure 6e illustrates different current densities at levels of 0.5, 1.0, 1.5, 2.0, and 2.5 A/g using perceived GCD profiles with a voltage range of 0−1.7 V. The following formula was used to calculate the mass load

$$\frac{w_+}{w_-} = \frac{C_{S-} \times V_-}{C_{S+} \times V_+} \quad (5)$$

where V signifies the potential range, w represents the mass, and C_S designates the specific capacitance. The C_s values for the ASC device (Figure 6f) were calculated to be 167, 159, 143, 107, and 79 F/g at current densities of 0.5, 1.0, 1.5, 2.0, and 2.5 A/g, respectively, according to the reported method.[39] In Figure 7a, the Ragone plots of the prepared ASC devices are presented, which were calculated by eqs S2 and S3 in the Supporting Information. The estimation reveals a maximum energy density of 67 Wh/kg at a power density of 1.05 kW/kg, and it can still sustain 31 Wh/kg at a high-power density of 5.29 kW/kg. The energy density is better or comparable to some previously reported supercapacitors with LTMDs or oxide/hydroxides as the electrode material, including Co_9S_8@NiO//AC (51.65 Wh/kg at 749.8 W/kg),[50] NiS/MoS_2@N-rGO//AC (35.69 Wh/kg and 601.8 W/kg),[51] $Zn_{0.76}Co_{0.24}S$@Ni_3S_2 (CSNAs)//AC (53.8 Wh/kg at a power density of 853 W/kg),[52] WS_2@$NiCo_2O_4$/CC//AC (45.67 Wh/kg at a power density of 992.83 W/kg),[53] and $Ni_{0.85}Se$@$MoSe_2$//AC (25.5 Wh/kg at a power density of 420 W/kg),[54] as decorated in Table S2. Superior capacitance is due to one-body $CoNiO_2$ NW geometry decorated on MoS_2 sheets possessing mechanical stability, making strong intimate contact between two materials and widening layer spaces. Accumulation of the core/shell interfaces provides ion-buffering reservoirs to enhance the ion/electron diffusion path lengths, ensuring good structural integrity/stability. The EIS results, as shown in Figure 7b, demonstrated that the $MoS_2/CoNiO_2$ ASC devices displayed a low R_{ct} of 0.85 Ω, indicating accelerated charge transfer and rapid reaction kinetics stemming from the synergistic interaction between materials. Figure 7c,d represents the schematic and photographic images of serially connected $MoS_2/CoNiO_2$-based ASC-based LED devices, respectively. The sequential LEDs (pink, green, and yellow) kept lighting for up to 20 min after 50 s of charging at about 3 V. The cycling robustness for $MoS_2/CoNiO_2$//AC was further examined up to 10 000 cycles at a current density of 2.5 A/g. As illustrated in Figure S11a, the device maintains a capacity retention of 94.1% relative to its initial capacitance after 10 000 cycles, revealing that vertically $CoNiO_2$ NWs grown on MoS_2 nanoflakes stimulate the fast ion transportation or insertion/extraction kinetics and support structural stability. The observed results suggested that, primarily, the assembled device realized low Coulombic efficiency (Figure S11b), whereas it achieved about 99% Coulombic efficiency in the ensuing sequences. These characteristics are credited to the enhanced absorption of electrolytic ions and the wettability of assembled devices for continuous cycling performance.[2]

4. CONCLUSIONS

In this work, the $CoNiO_2$ NWs with multiple edge sites are connected to MoS_2 nanoflakes via a hydrothermal process to improve the conductivity and enhance the material's surface area, which is advantageous for accommodating charge accumulation and facilitating electron/ion transport and electrochemistry activity of hierarchical porous nanowire-like MoS_2@$CoNiO_2$ nanohybrids. Taking advantage of the hierarchical 3D porous/NWs architecture and the collaborative effects of active materials, the $MoS_2/CoNiO_2$ half-cell electrode displays a high specific capacitance of 1340 F/g at a current density of 0.5 A/g along with 95.6% retention over 10 000 cycles. Based on this, $MoS_2/CoNiO_2$//AC achieves a high specific capacitance of 167 F/g at 0.5 A/g along with an outstanding energy density of 67 Wh/kg at a power density of 1.05 kW/kg. This work offers a promising direction for the fabrication of abundant active sites and hierarchical porous nanowire-like nanocomposites for energy storage applications.

■ ASSOCIATED CONTENT

Supporting Information

The Supporting Information is available free of charge at https://pubs.acs.org/doi/10.1021/acsami.3c17201.

Characterization information; electrochemical equations; comparison tables; survey XPS profiles, elemental and mapping analysis; BET and BJH analysis results; comparative electrochemical performances of MoS_2, $CoNiO_2$, and $MoS_2/CoNiO_2$; capacitive behavior calculation results; EIS with the fitted circuit; stability GCD profiles and retention curves; SEM, compositional, and elemental mapping of the hybrid before and after stability; and electrochemical results of activated carbon (PDF)

■ AUTHOR INFORMATION

Corresponding Authors

Sajjad Hussain − *Hybrid Materials Center (HMC) and Department of Nanotechnology and Advanced Materials Engineering, Sejong University, Seoul 05006, Korea;* orcid.org/0000-0002-0035-9975; Email: shussainawan@gmail.com

Deok-Kee Kim − *Department of Electrical Engineering and Convergence Engineering for Intelligent Drone, Sejong University, Seoul 05006, Korea; Department of Semiconductor Systems Engineering, Sejong University, Seoul 05006, Korea;* orcid.org/0000-0002-2515-4984; Email: deokkeekim@sejong.ac.kr

Authors

Zulfqar Ali Sheikh − *Department of Electrical Engineering and Convergence Engineering for Intelligent Drone, Sejong University, Seoul 05006, Korea*

Dhanasekaran Vikraman − *Division of Electronics and Electrical Engineering, Dongguk University—Seoul, Seoul 04620, Korea;* orcid.org/0000-0001-8991-3604

https://doi.org/10.1021/acsami.3c17201
ACS Appl. Mater. Interfaces 2024, 16, 10104−10115

Muhammad Faizan − *Department of Energy & Materials Engineering, Dongguk University—Seoul, Seoul 04620, Korea*
Honggyun Kim − *Department of Semiconductor Systems Engineering, Sejong University, Seoul 05006, Korea*
Sikandar Aftab − *Department of Intelligent Mechatronics Engineering, Sejong University, Seoul 05006, Korea;* orcid.org/0000-0003-2184-4598
Shoyebmohamad F. Shaikh − *Department of Chemistry, College of Science, King Saud University, Riyadh 11451, Saudi Arabia*
Kyung-Wan Nam − *Department of Energy & Materials Engineering, Dongguk University—Seoul, Seoul 04620, Korea;* orcid.org/0000-0001-6278-6369
Jongwan Jung − *Hybrid Materials Center (HMC) and Department of Nanotechnology and Advanced Materials Engineering, Sejong University, Seoul 05006, Korea;* orcid.org/0000-0002-1397-212X

Complete contact information is available at: https://pubs.acs.org/10.1021/acsami.3c17201

Notes

The authors declare no competing financial interest.

■ ACKNOWLEDGMENTS

This research was supported by the National Research Foundation of Korea (NRF), funded by the Ministry of Science and ICT (2022M3I7A4072293 and 2016R1D1A1B01009537). The authors extend their appreciation to the Deputyship for Research and Innovation, "Minstry of Education" in Saudi Arabia for funding this research (IFKSUOR3-294-3).

■ REFERENCES

(1) Numan, A.; Iqbal, J.; Jagadish, P.; Krishnan, S. G.; Khalid, M.; Pannipara, M.; Wageh, S. Tailoring Crystallinity of 2D Cobalt Phosphate to Introduce Pseudocapacitive Behavior. *J. Energy Storage* **2022**, *54*, No. 105371.
(2) Karuppasamy, K.; Vikraman, D.; Hussain, S.; Thirumalraj, B.; Santhoshkumar, P.; Parangusan, H.; Park, H.-C.; Jung, J.; Kim, H.-S. Unveiling The Redox Electrochemistry Of 1D, Urchin-Like Vanadium Sulfide Electrodes For High-Performance Hybrid Supercapacitors. *J. Energy Chem.* **2023**, *79*, 569−580.
(3) Santhoshkumar, P.; Vikraman, D.; Hussain, S.; Karuppasamy, K.; Kathalingam, A.; Kim, H.-S. 3D-Architectured Spherical $Ce_2Mo_5O_{16}$ by a Time-Dependent Hydrothermal Process and Their Energy Storage Application. *J. Alloys Compd.* **2022**, *928*, No. 167215.
(4) Vikraman, D.; Hussain, S.; Rabani, I.; Feroze, A.; Ali, M.; Seo, Y.-S.; Chun, S.-H.; Jung, J.; Kim, H.-S. Engineering $MoTe_2$ and Janus SeMoTe nanosheet structures: First-principles Roadmap and Practical Uses in Hydrogen Evolution Reactions and Symmetric Supercapacitors. *Nano Energy* **2021**, *87*, No. 106161.
(5) Alrwashdeh, M.; Alameri, S. A. SiC and FeCrAl as Potential Cladding Materials for APR-1400 Neutronic Analysis. *Energies* **2022**, *15* (10), 3772.
(6) Alrwashdeh, M.; Alameri, S. A.; Alkaabi, A. K. Preliminary Study of a Prismatic-Core Advanced High-Temperature Reactor Fuel Using Homogenization Double-Heterogeneous Method. *Nucl. Sci. Eng.* **2020**, *194* (2), 163−167.
(7) Peng, Z.; Jia, D.; Tang, J.; Wang, Y.; Wang, Y.; Zhang, L.; Zheng, G. $CoNiO_2$/TiN−TiO_xN_y Composites For Ultrahigh Electrochemical Energy Storage and Simultaneous Glucose Sensing. *J. Mater. Chem. A* **2014**, *2* (28), 10904−10909.
(8) Hung, P.-S.; Chung, W.-A.; Chou, S.-C.; Tso, K.-C.; Chang, C.-K.; Wang, G.-R.; Guo, W.-Q.; Weng, S.-C.; Wu, P.-W. Composite $NiCoO_2/NiCo_2O_4$ inverse opals for the oxygen evolution reaction in an alkaline electrolyte. *Catal. Sci. Technol.* **2020**, *10* (22), 7566−7580.
(9) Hussain, S.; Vikraman, D.; Abbas, Z.; Faizan, M.; Aftab, S.; Batoo, K. M.; Kim, H.-S.; Nam, K.-W.; Jung, J. Hierarchical Dessert Plant-Like $CoNiO_2$ Nanowires Decoration On MoS_2 Nano-Petals For Enhanced Bi-Functional Overall Water Splitting Reactions. *Sustainable Mater. Technol.* **2023**, *37*, No. e00696.
(10) Zhou, J.; Dou, Y.; Zhou, A.; Shu, L.; Chen, Y.; Li, J.-R. Layered Metal−Organic Framework-Derived Metal Oxide/Carbon Nanosheet Arrays for Catalyzing the Oxygen Evolution Reaction. *ACS Energy Lett.* **2018**, *3* (7), 1655−1661.
(11) Xiong, S.; Chen, J. S.; Lou, X. W.; Zeng, H. C. Mesoporous Co_3O_4 and CoO@C topotactically transformed from chrysanthemum-like $Co(CO_3)_{0.5}(OH)\cdot 0.11\ H_2O$ and their lithium-storage properties. *Adv. Funct. Mater.* **2012**, *22* (4), 861−871.
(12) Zhen, C.; Zhang, X.; Wei, W.; Guo, W.; Pant, A.; Xu, X.; Shen, J.; Ma, L.; Hou, D. Nanostructural Origin of Semiconductivity and Large Magnetoresistance in Epitaxial $NiCo_2O_4/Al_2O_3$ Thin Films. *J. Phys. D: Appl. Phys.* **2018**, *51* (14), No. 145308.
(13) Gao, Z.; Song, N.; Li, X. Microstructural Design of Hybrid CoO@NiO and Graphene Nano-Architectures for Flexible High Performance Supercapacitors. *J. Mater. Chem. A* **2015**, *3* (28), 14833−14844.
(14) Li, H.; Fu, H.; Yu, J.; Wang, L.; Shi, Y.; Chen, L. Urchin-like $CoNiO_2$ Microspheres Supported on Reduced Graphene Oxide with N and S co-doped for Overall Water Splitting with Trace Load as The bifunctional electrocatalyst. *J. Alloys Compd.* **2022**, *922*, No. 166254.
(15) Pan, Z.-Y.; Tang, Z.; Zhan, Y.-Z.; Sun, D. Three-dimensional Porous $CoNiO_2$@reduced Graphene Oxide Nanosheet Arrays/Nickel Foam as a Highly Efficient Bifunctional Electrocatalyst For Overall Water Splitting. *Tungsten* **2020**, *2*, 390−402.
(16) Pu, J.; Gong, W.; Shen, Z.; Wang, L.; Yao, Y.; Hong, G. $CoNiO_2/Co_4N$ Heterostructure Nanowires Assisted Polysulfide Reaction Kinetics For Improved Lithium−Sulfur Batteries. *Adv. Sci.* **2022**, *9* (4), No. 2104375.
(17) Leng, X.; Shao, Y.; Wu, L.; Wei, S.; Jiang, Z.; Wang, G.; Jiang, Q.; Lian, J. A Unique Porous Architecture Built By Ultrathin Wrinkled $NiCoO_2$/rGO/$NiCoO_2$ Sandwich Nanosheets For Pseudocapacitance and Li Ion Storage. *J. Mater. Chem. A* **2016**, *4* (26), 10304−10313.
(18) Liu, G.-B.; Xiao, D.; Yao, Y.; Xu, X.; Yao, W. Electronic Structures and Theoretical Modelling of Two-Dimensional Group-VIB Transition Metal Dichalcogenides. *Chem. Soc. Rev.* **2015**, *44* (9), 2643−2663.
(19) Xie, L. M. Two-Dimensional Transition Metal Dichalcogenide Alloys: Preparation, Characterization And Applications. *Nanoscale* **2015**, *7* (44), 18392−18401.
(20) Rasamani, K. D.; Alimohammadi, F.; Sun, Y. Interlayer-Expanded MoS_2. *Mater. Today* **2017**, *20* (2), 83−91.
(21) Mao, J.; Wang, Y.; Zheng, Z.; Deng, D. The Rise of Two-Dimensional MoS_2 for Catalysis. *Front. Phys.* **2018**, *13* (4), No. 138118.
(22) Yu, L.; Lee, Y.-H.; Ling, X.; Santos, E. J. G.; Shin, Y. C.; Lin, Y.; Dubey, M.; Kaxiras, E.; Kong, J.; Wang, H.; Palacios, T. Graphene/MoS_2 Hybrid Technology for Large-Scale Two-Dimensional Electronics. *Nano Lett.* **2014**, *14* (6), 3055−3063.
(23) Wei, S.; Fu, Y.; Liu, M.; Yue, H.; Park, S.; Lee, Y. H.; Li, H.; Yao, F. Dual-phase MoS_2/MXene/CNT ternary Nanohybrids For Efficient Electrocatalytic Hydrogen Evolution. *npj 2D Mater. Appl.* **2022**, *6* (1), 25.
(24) Deng, H.; Zhang, C.; Xie, Y.; Tumlin, T.; Giri, L.; Karna, S. P.; Lin, J. Laser induced MoS_2/carbon hybrids for hydrogen evolution reaction catalysts. *J. Mater. Chem. A* **2016**, *4* (18), 6824−6830.
(25) Faizan, M.; Hussain, S.; Vikraman, D.; Ali, B.; Kim, H.-S.; Jung, J.; Nam, K.-W. MoS_2@Mo_2C Hybrid Nanostructures Formation as an Efficient Anode Material For Lithium-Ion Batteries. *J. Mater. Res.Technol.* **2021**, *14*, 2382−2393.
(26) Tang, T.; Gan, Q.; Guo, X.; Dong, H.; Zhang, J.; Zhao, Y.; Tian, J.; Yang, X. A Hybrid Catalyst of Pt/$CoNiO_2$ on Carbon

Nanotubes and its Synergetic Effect Towards Remarkable Ethanol Electro-Oxidation in Alkaline Media. *Sustainable Energy Fuels* **2018**, *2* (1), 229−236.
(27) Ren, Z.; Li, J.; Ren, Y.; Wang, S.; Qiu, Y.; Yu, J. Large-Scale Synthesis of Hybrid Metal Oxides Through Metal Redox Mechanism For High-Performance Pseudocapacitors. *Sci. Rep.* **2016**, *6* (1), 20021.
(28) Vikraman, D.; Park, H. J.; Kim, S. I.; Thaiyan, M. Magnetic, Structural And Optical Behavior of Cupric Oxide Layers For Solar Cells. *J. Alloys Compd.* **2016**, *686*, 616−627.
(29) Yang, X.; Li, H.; Lu, A.-Y.; Min, S.; Idriss, Z.; Hedhili, M. N.; Huang, K.-W.; Idriss, H.; Li, L.-J. Highly Acid-Durable Carbon Coated Co_3O_4 nanoarrays as Efficient Oxygen Evolution Electrocatalysts. *Nano Energy* **2016**, *25*, 42−50.
(30) Patil, S. A.; Rabani, I.; Vikraman, D.; Bathula, C.; Shrestha, N. K.; Kim, H.; Hussain, S.; Im, H. Template-Free Synthesis of One-Dimensional Cobalt Sulfide Nanorod Array as an Attractive Architecture For Overall Water Splitting. *Int. J. Energy Res.* **2021**, *45* (2), 2785−2796.
(31) Feng, Y.; Yu, X.-Y.; Paik, U. Nickel Cobalt Phosphides Quasi-Hollow Nanocubes as an Efficient Electrocatalyst For Hydrogen Evolution In Alkaline Solution. *Chem. Commun.* **2016**, *52* (8), 1633−1636.
(32) Ye, J.; Chen, L.; Shi, Y.; Hou, J.; Kong, W.; Gu, T.; Jiang, R.; Wang, L.; Luo, Y.; Guo, X. Crystalline-Amorphous Hybrid $CoNiO_2$ Nanowires with Enhanced Capacity and Energy Density for Aqueous Zinc-Ion Hybrid Supercapacitors. *ACS Appl. Energy Mater.* **2021**, *4* (11), 12345−12352.
(33) Pan, F.-C.; He, H.; Yang, Z.-X.; Zheng, Q.; Lin, D.; Huo, Y. Rationally Designed $Ni_2P/WS_2/Co_9S_8$@C Multi-Interfacial Electrocatalyst For Efficient Overall Water Splitting. *Chem. Eng. J.* **2022**, *446*, No. 136961.
(34) Song, I.; Park, C.; Hong, M.; Baik, J.; Shin, H. J.; Choi, H. C. Patternable Large-Scale Molybdenium Disulfide Atomic Layers Grown By Gold-Assisted Chemical Vapor Deposition. *Angew. Chem.* **2014**, *126* (5), 1290−1293.
(35) Wu, Z.; Li, B.; Xue, Y.; Li, J.; Zhang, Y.; Gao, F. Fabrication of Defect-rich MoS_2 Ultrathin Nanosheets For Application In Lithium-Ion Batteries And Supercapacitors. *J. Mater. Chem. A* **2015**, *3* (38), 19445−19454.
(36) Kumar, L.; Chauhan, H.; Yadav, N.; Yadav, N.; Hashmi, S. A.; Deka, S. Faster Ion Switching $NiCo_2O_4$ Nanoparticle Electrode-Based Supercapacitor Device With High Performances And Long Cycling Stability. *ACS Appl. Energy Mater.* **2018**, *1* (12), 6999−7006.
(37) Katkar, P. K.; Padalkar, N. S.; Patil, A. M.; Jeon, J. H.; Sheikh, Z. A.; Jerng, S. K.; Na, H. R.; Lee, S.; Chun, S. H. Development of amorphous Fe-doped nickel-cobalt phosphate ($Fe_xNiCo(PO_4)_2$) nanostructure for enhanced performance of solid-state asymmetric supercapacitors. *Int. J. Energy Res.* **2022**, *46* (9), 12039−12056.
(38) Yang, P.; Wu, Z.; Jiang, Y.; Pan, Z.; Tian, W.; Jiang, L.; Hu, L. Fractal $(Ni_xCo_{1-x})_9Se_8$ Nanodendrite Arrays with Highly Exposed () Surface for Wearable, All-Solid-State Supercapacitor. *Adv. Energy Mater.* **2018**, *8* (26), No. 1801392.
(39) Vikraman, D.; Hussain, S.; Karuppasamy, K.; Santhoshkumar, P.; Kathalingam, A.; Jung, J.; Kim, H.-S. Fabrication of Asymmetric Supercapacitors Using Molybdenum Dichalcogenide Nanoarray Structures. *Int. J. Energy Res.* **2022**, *46* (13), 18410−18425.
(40) Kour, P.; Yadav, K. Electrochemical Performance Of Mixed-Phase 1T/2H MoS_2 synthesized By Conventional Hydrothermal V/S Microwave-Assisted Hydrothermal Method For Supercapacitor Applications. *J. Alloys Compd.* **2022**, *922*, No. 166194.
(41) Qu, C.; Cao, J.; Chen, Y.; Wei, M.; Fan, H.; Liu, X.; Li, X.; Wu, Q.; Feng, B.; Yang, L. In-situ Growth of hierarchical Trifunctional Co_4S_3/Ni_3S_2@MoS_2 core-Shell Nanosheet Array On Nickel Foam For Overall Water Splitting And Supercapacitor. *Int. J. Hydrogen Energy* **2023**, *48* (2), 648−661.
(42) Chen, L.; Deng, W.; Chen, Z.; Wang, X. Hetero-architectured Core−shell $NiMoO_4$@Ni_9S_8/MoS_2 Nanorods Enabling High-Performance Supercapacitors. *J. Mater. Res.* **2022**, *37*, 284−293.
(43) Li, X.; Lin, Z.; Wei, Y.; Luo, W.; Ding, J.; Li, T.; Ma, Y. MXene-MnO_2-CoNi Layered Double Hydroxides//Activated Carbon Flexible Asymmetric Supercapacitor. *J. Energy Storage* **2022**, *55*, No. 105668.
(44) Bokhari, S. W.; Wei, S.; Gao, W. Synthesis of bimetallic MoS_2/VS_2 Nano-Urchins-Reduced Graphene Oxide Hybrid Nanocomposite For High Performance Supercapacitor Application. *Electrochim. Acta* **2021**, *398*, No. 139300.
(45) Kour, P.; Kour, S.; Sharma, A. L.; Yadav, K. Synergistic Improvement In Electrochemical Performance of Cr-Doped MoS_2/$CuCo_2S_4$ Binary Composite For Hybrid Supercapacitors. *Fuel* **2024**, *358*, No. 130173.
(46) Lee, S.; Hwang, J.; Kim, D.; Ahn, H. Oxygen Incorporated in 1T/2H Hybrid MoS_2 Nanoflowers Prepared From Molybdenum Blue Solution For Asymmetric Supercapacitor Applications. *Chem. Eng. J.* **2021**, *419*, No. 129701.
(47) Zeng, R.; Li, Z.; Li, L.; Li, Y.; Huang, J.; Xiao, Y.; Yuan, K.; Chen, Y. Covalent Connection of Polyaniline with MoS_2 Nanosheets towards Ultrahigh Rate Capability Supercapacitors. *ACS Sustainable Chem. Eng.* **2019**, *7* (13), 11540−11549.
(48) Ray, S. K.; Pant, B.; Park, M.; Hur, J.; Lee, S. W. Cavity-like hierarchical architecture of WS_2/α-NiMoO4 electrodes for supercapacitor application. *Ceram. Int.* **2020**, *46* (11), 19022−19027.
(49) Kasinathan, D.; Prabhakar, P.; Muruganandam, P.; Wiston, B. R.; Mahalingam, A.; Sriram, G. Solution Processed NiO/MoS_2 Heterostructure Nanocomposite for Supercapacitor Electrode Application. *Energies* **2023**, *16* (1), 335.
(50) Wang, J.; Huang, Y.; Han, X.; Zhang, S.; Wang, M.; Yan, J.; Chen, C.; Zong, M. Construction of Hierarchical Co_9S_8@NiO Synergistic Microstructure For High-Performance Asymmetric Supercapacitor. *J. Colloid Interface Sci.* **2021**, *603*, 440−449.
(51) Xu, X.; Zhong, W.; Zhang, X.; Dou, J.; Xiong, Z.; Sun, Y.; Wang, T.; Du, Y. Flexible Symmetric Supercapacitor With Ultrahigh Energy Density Based on NiS/MoS_2@N-rGO Hybrids Electrode. *J. Colloid Interface Sci.* **2019**, *543*, 147−155.
(52) Lv, Y.; Liu, A.; Shi, Z.; Che, H.; Mu, J.; Guo, Z.; Zhang, X. Construction Of Hierarchical Zinc Cobalt Sulfide@Nickel Sulfide Core-Shell Nanosheet Arrays For High-Performance Asymmetric Solid-State Supercapacitors. *Chem. Eng. J.* **2018**, *349*, 397−407.
(53) Li, L.; Gao, J.; Cecen, V.; Fan, J.; Shi, P.; Xu, Q.; Min, Y. Hierarchical WS_2@$NiCo_2O_4$ Core−shell Heterostructure Arrays Supported on Carbon Cloth as High-Performance Electrodes for Symmetric Flexible Supercapacitors. *ACS Omega* **2020**, *5* (9), 4657−4667.
(54) Peng, H.; Wei, C.; Wang, K.; Meng, T.; Ma, G.; Lei, Z.; Gong, X. $Ni_{0.85}Se$@$MoSe_2$ Nanosheet Arrays as the Electrode For High-Performance Supercapacitors. *ACS Appl. Mater. Interfaces* **2017**, *9* (20), 17067−17075.

https://doi.org/10.1021/acsami.3c17201
ACS Appl. Mater. Interfaces 2024, 16, 10104−10115